Available online at www.sciencedirect.com
SCIENCE DIRECT®
Journal of volcanology and geothermal research
ELSEVIER
Journal of Volcanology and Geothermal Research 129 (2004) 7–22
www.elsevier.com/locate/jvolgeores

Bubble growth during decompression of magma: experimental and theoretical investigation

N.G. Lensky [a,*], O. Navon [b], V. Lyakhovsky [a]

[a] *Geological Survey of Israel, 30 Malkhe Yisrael Street, Jerusalem 95501, Israel*
[b] *Institute of Earth Sciences, The Hebrew University of Jerusalem, Jerusalem 91904, Israel*

Abstract

A model of bubble growth during decompression of supersaturated melt was developed in order to explore the conditions for preservation of gas overpressure in bubbles or for maintaining supersaturation of the melt. The model accounts for the interplay of three dynamic processes: decompression rate of the magma, deformation of the viscous melt around the growing bubble, and diffusion of volatiles into the bubble. Generally, these processes are coupled and the evolution of bubble radius and gas pressure is solved numerically. For a better understanding of the physics of the processes, we developed some analytical solutions under simplifying assumptions for cases where growth is controlled by viscous resistance, diffusion or linear decompression rate. We show that the solutions are a function of time and two dimensionless numbers, which are the ratios of either the diffusive or viscous time scales over the decompression time scale. The conditions for each growth regime are provided as a function of the two governing dimensionless parameters. Analytical calculations for some specific cases compare well with numerical simulations and experimental results on bubble growth during decompression of hydrated silicic melts. The model solutions, including the division to the growth regimes as function of the two parameters, provide a fast tool for estimation of the state of erupting magma in terms of gas overpressure, supersaturation and gas volume fraction. The model results are in agreement with the conditions of Plinian explosive eruption (e.g. Mount St. Helens, 18 May 1980), where high gas overpressure is expected. The conditions of effusion of lava domes with sudden onset of explosive activity are also in agreement with the model predictions, mostly in equilibrium degassing and partly in overpressure conditions. We show that in a situation of quasi-static diffusion during decompression the diffusive influx depends on the diffusivity away from the bubble, insensitive to the diffusivity profile.

Keywords: bubble growth; decompression; viscosity; diffusion; magma

1. Introduction

Volcanic eruptions commonly involve formation and growth of gas bubbles. The growth dynamics play a major role in determining the style of eruption. Current bubble growth models are based on the formulation of Rayleigh (1917) and Scriven (1959) that accounted for the fluid dynamics of an incompressible viscous liquid around an isolated spherical bubble with pressure difference between bubble and the surrounding liquid. Bubble growth in highly silicic melts is

* Corresponding author. Tel.: +972-2-531-4259; Fax: +972-2-566-2581.
E-mail addresses: nadavl@mail.gsi.gov.il (N.G. Lensky), oded.navon@huji.ac.il (O. Navon), vladi@geos.gsi.gov.il (V. Lyakhovsky).

0377-0273/03/$ – see front matter © 2003 Elsevier B.V. All rights reserved.
doi:10.1016/S0377-0273(03)00229-4

characterized by mass flux of volatiles from the supersaturated melt into the bubble and by high viscosity of the melt. These effects were accounted for by Sparks (1978), and the effect of neighboring bubbles and variable melt properties were also developed (Toramaru, 1989; Proussevitch et al., 1993; Toramaru, 1995; Lyakhovsky et al., 1996; Navon et al., 1998; Proussevitch and Sahagian, 1998).

Two characteristic time scales arise from the governing equations for growth under constant pressure: the time for viscous deformation, τ_{vis}, which is an estimation of the time it takes to relax gas overpressure, and the time for diffusion of volatiles into the bubble, τ_{dif} (Navon and Lyakhovsky, 1998). The ratio between these two characteristic time scales is the non-dimensional Peclet number. Three end-member growth regimes were characterized during the course of bubble growth. At the initial stages of growth, diffusion is very efficient and preserves gas pressure close to its initial hydration pressure. Growth is then controlled by the viscous deformation of the melt around the bubble and follows an exponent of time (Navon et al., 1998). After a time on the order of the viscous time scale, gas pressure drops and approaches ambient pressure. Growth is then controlled by the diffusive flux of volatiles and bubble growth follows a square root of time (Lyakhovsky et al., 1996). Finally, the bubbles approach their final radius, which is a function of the ambient pressure, initial volatile content and initial separation between bubbles. The model produces good fits to experiments where bubbles grew under constant ambient pressure (Navon and Lyakhovsky, 1998). The effect of gradual decompression on bubble growth was accounted for by numerical simulations (Toramaru, 1995; Proussevitch and Sahagian, 1996; Navon and Lyakhovsky, 1998; Blower et al., 2001). Yet, there are no analytical solutions and experimental verifications of the model under conditions of continuous decompression, which is the common case in volcanic systems.

During continuous decompression of magma, bubble growth is also governed by the decompression rate, in addition to the viscous deformation and diffusion. Accordingly, a third characteristic time scale, the time needed to fully release ambient pressure by linear decompression, should be introduced. As a result, two dimensionless numbers characterize the growth dynamics, which are the ratios between diffusion and decompression time scales, and between the viscous resistance and decompression time scales, instead of the Peclet number. We present analytical solutions of the bubble growth model under falling ambient pressure, and characterize the conditions for each growth regime in terms of the two dimensionless numbers. We compare the analytical results with numerical simulations and experiments on bubble growth during decompression of hydrated silicic melts. In order to test the analytical model solutions we conducted bubble growth experiments and also use the results of Gardner et al. (1999).

2. Theory of bubble growth during decompression of volatile bearing magma

A suspension of bubbles in a viscous liquid is approximated by a close pack of spherical cells, each consisting of a gas bubble of radius R surrounded by a spherically symmetric melt shell with outer radius S (Fig. 1). The cells are arranged in space with some overlaps and some voids (Proussevitch et al., 1993), so that the volume fraction of gas in the magma, α, is:

$$\alpha = (R/S)^3 \tag{1}$$

This geometrical arrangement allows describing the whole magma by examining the dynamics of a single spherical cell, using equations developed for a solitary bubble (Scriven, 1959; Sparks, 1978) and former cell models (Toramaru, 1989; Proussevitch et al., 1993; Toramaru, 1995; Lyakhovsky et al., 1996; Navon and Lyakhovsky, 1998; Proussevitch and Sahagian, 1998). The model presented here is based on the formulation of Proussevitch et al. (1993).

Mass conservation of the melt is ensured by the continuity equation, which for an incompressible melt is simply $\mathrm{div}(v) = 0$, where v is the velocity field at the melt shell. Integration of the equation of continuity for the radial velocity in the melt, v_r,

around a bubble growing at the rate $\dot{R}$ (see Fig. 1 for notations) yields:

$$v_r = \dot{R}\frac{R^2}{r^2}(R \leq r \leq S) \tag{2}$$

Navier–Stokes equation (equation of motion) states that the total pressure in the bubble (P_{gas}) is the sum of ambient pressure (P_{amb}), surface tension (σ) and viscous stresses due to the deformation of the melt shell:

$$P_{gas} = P_{amb} + \frac{2\sigma}{R} + 4\frac{\dot{R}}{R}\eta_{eff} \tag{3}$$

where η_{eff} is the effective viscosity that resists bubble expansion, which accounts for the effects of finite shell size and variable viscosity (Lensky et al., 2001):

$$\eta_{eff} = \eta_R\left[1 - \frac{\eta_S}{\eta_R}\alpha + \frac{R^3}{\eta_R}\int_R^S \frac{d\eta}{dr}\frac{1}{r^3}dr\right] \tag{3a}$$

Inertial terms are usually negligible compared with the viscous terms in most magmatic situations as indicated by small Reynold's number, $Re \equiv (\dot{R}R\rho_{melt})/(\eta) \ll 1$. The evolution of bubble size is implicitly determined using Eq. 3 when gas pressure is known (as will be discussed below, in Sections 3.2 and 3.7). However, in the case of volatile bearing magmas, diffusive influx from the supersaturated melt has to be considered. Volatile mass balance between bubbles and melt is:

$$\frac{4\pi}{3}\frac{d}{dt}(\rho_{gas}R^3) = 4\pi\rho_{melt}\left(r^2 D\frac{\partial C}{\partial r}\right)_{r=R} \tag{4}$$

where ρ_{gas} and ρ_{melt} are gas and melt densities, D is volatile diffusivity in the melt and C is the weight fraction of volatiles in the melt. Gas density is related to gas pressure through the equation of state, assuming an ideal gas of molar mass M, gas constant G and constant temperature T:

$$\rho_{gas} = P_{gas}\frac{M}{GT} \tag{5}$$

To solve the concentration gradient (the right side of Eq. 4), we consider the diffusion–advection equation:

$$\frac{dC}{dt} = \frac{1}{r^2}\frac{\partial}{\partial r}\left(r^2 D\frac{\partial C}{\partial r}\right) \tag{6}$$

where $d/dt = (\partial)/(\partial t) + v_r(\partial)/(\partial r)$. The equation is subjected to two boundary conditions. At the bubble–melt interface, R, water concentration is locally in equilibrium with the gas pressure through the Henry's law relation (Burnham, 1975):

$$C_R = K_H P_{gas}^n \tag{7}$$

where K_H is Henry's constant and $n \approx 0.5$ for water in silicic melts. The second condition derives from the requirement of volatile mass conservation in the cell, which states that the mass of volatiles in the bubble plus the mass dissolved in the melt equals the constant total (or initial) mass of volatiles in the cell:

$$\frac{4}{3}\pi R^3\rho_{gas} + \int_R^S 4\pi r^2\rho_{melt}C dr = \frac{4}{3}\pi S_0^3\rho_{melt}C_0 \tag{8}$$

where $(4/3)\pi S_0^3 = (4/3)\pi S^3(t) - (4/3)\pi R^3(t)$ is the volume of the incompressible melt shell when the bubble vanishes ($R \to 0$), and C_0 is the concentration of volatiles in the melt under this condition. The condition of mass conservation may also be expressed as a no mass flux condition at the outer boundary S:

$$\frac{\partial C}{\partial r}|_{r=s} = 0 \tag{8a}$$

Taken together, Eqs. 2–8 define a set of equations and boundary conditions which, at present, calls for a numerical solution. For a better understanding of the physics of the processes, we present some analytical solutions under simplifying assumptions for some specific cases.

3. Model solutions

3.1. Scaling

Non-dimensionalization allows simplification of the formulations and clarification of the parameter dependencies and their importance in each process. In Table 1 the fluid properties and other physical parameters are transformed into a non-dimensional form. Three different time scales that relate to the three governing processes (decompression, viscous resistance, and volatile diffusion)

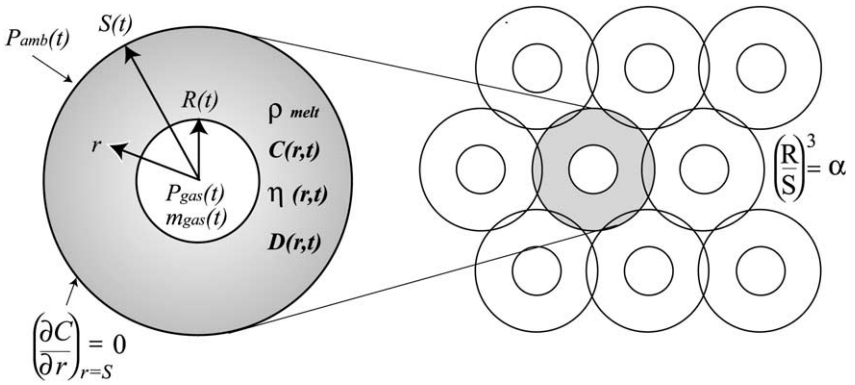

Fig. 1. The physical model. The magma is regarded as a pack of spherical cells, each composed of a gas bubble with radius R centered in a spherical melt shell with outer radius S. The cells are arranged in a 3-D lattice with some overlap, so that gas volume fraction is $\alpha=(R/S)^3$. (Modified after Proussevitch et al., 1993).

include the important natural variables, as defined in Table 1. Decompression time scale, $\tau_{dec}=(P_i)/(\dot{P}_{amb})$, is the time it takes to decompress magma from initial pressure to zero final pressure, where $\dot{P}_{amb}$ denotes constant (or average) decompression rate. Time is scaled to the decompression time scale and is in the range $0\leq\hat{t}\leq(t_f)/(\tau_{dec})$, where t_f is the time when the final ambient pressure is reached (in cases where pressure is not fully released). Here and throughout the paper, hat symbols denote dimensionless variables. The viscous time scale,

Table 1
The governing variables and their scaling

Variable	Notation	Units	Scaled to	Non-dimensional
Pressure	P	Pa	Initial pressure P_i	$\hat{P}=\frac{P}{P_i}$
Gas density	ρ_{gas}	Kg m^{-3}	Initial gas density ρ_i	$\hat{\rho}_{gas}=\frac{\rho_{gas}}{\rho_i}=\hat{P}_{gas}$
Melt density	ρ_{melt}	Kg m^{-3}	Initial gas density ρ_i	$\hat{\rho}_{melt}=\frac{\rho_{melt}}{\rho_i}$
Bubble radius	R	m	Initial radius R_i	$\hat{R}=\frac{R}{R_i}$
Surface tension	σ	Pa m	R_i,P_i	$\Sigma=2\frac{\sigma}{R_i}\frac{1}{P_i}$
Diffusivity[a]	D	m^2 s^{-1}	Initial density D_i	$\hat{D}=\frac{D}{D_i}$
Viscosity[b]	η_{eff}	Pa s	Initial viscosity η_i	$\hat{\eta}_{eff}=\frac{\eta_R}{\eta_i}\left[1-\frac{\eta_S}{\eta_R}\alpha+\frac{R^3}{\eta_R}\int_R^S\frac{d\eta}{dr}\frac{1}{r^3}dr\right]$
Decompression time scale	$\tau_{dec}=\frac{P_i}{\dot{P}_{amb}}$	s		
Time	t	s	$\tau_{dec}=\frac{P_i}{\dot{P}_{amb}}$	$\hat{t}=\frac{t}{\tau_{dec}}$
Viscous time scale	$\tau_{vis}=\frac{4\eta_i}{P_i}$	s	$\tau_{dec}=\frac{P_i}{\dot{P}_{amb}}$	$\Theta_V=\frac{\tau_{vis}}{\tau_{dec}}$
Diffusion time scale	$\tau_{dif}=\frac{R_i^2}{D_i}$	s	$\tau_{dec}=\frac{P_i}{\dot{P}_{amb}}$	$\Theta_D=\frac{\tau_{dif}}{\tau_{dec}}$
Growth velocity	$\dot{R}$	m s^{-1}	$\frac{\tau_{dec}}{R_i}$	$\hat{\dot{R}}=\dot{R}\frac{\tau_{dec}}{R_i}$

[a] When diffusivity is constant $\hat{D}=1$.
[b] When viscosity is constant $\eta=1-;\alpha$, and when vesicularity is low $\eta\sim1$.

$\tau_{vis} = (4\eta_i)/(P_i)$, is a measure for the time for viscous relaxation of gas overpressure. Diffusion time scale $\tau_{dif} = (R_i^2)/(D_i)$, characterizes the diffusive mass transfer in the melt around a bubble with a radius R_i at the initial stages. The upper bound for the time it takes to diffuse water from the whole shell to the bubble can be approximated as $\tau_{dif}((S_0^2)/(R_1^2))$, where S_0 is the thickness of the melt shell when the bubble vanishes, $S_0 = (S^3 - R^3)^{1/3} = const$ (Fig. 1).

The physical variables are condensed into two dimensionless parameters that are the ratios between these viscous and diffusion time scales to the decompression time scale $\Theta_V = (\tau_{vis})/(\tau_{dec}) = (4\eta_i \dot{P}_{amb})/(P_i^2)$ and $\Theta_D = (\tau_{dif})/(\tau_{dec}) = (R_i^2 \dot{P}_{amb})/(DP_i)$, similar to the parameters used by Toramaru (1995). These two parameters become larger as decompression rate increases. Dehydration also leads to higher values of both parameters since viscosity increases and diffusivity decreases.

3.2. The governing equations in non-dimensional form

Using the above scaling scheme, Eqs. 3–8 are rewritten in their non-dimensional form (for notations see Table 1).

Eq. 3 transforms to:

$$\hat{P}_{gas} = \hat{P}_{amb} + \frac{\Sigma}{\hat{R}} + \Theta_V \frac{\dot{\hat{R}}}{\hat{R}} \hat{\eta}_{eff} \tag{9}$$

For constant decompression rate we define the ambient pressure as:

$$\hat{P}_{amb} = 1 - \hat{t} \tag{10}$$

where, as noted, $1 \geq \hat{P}_{amb} \geq (P_f/P_i) > 0$ and P_f is the final ambient pressure. The equation of mass balance (Eq. 4) transforms to:

$$\frac{1}{\tau_{dec}} \frac{d}{d\hat{t}} (\hat{P}_{gas} \hat{R}^3) = \frac{3}{\tau_{dif}} \hat{\rho}_{melt} \left(\hat{r}^2 \hat{D} \frac{\partial C}{\partial \hat{r}} \right)_{\hat{r}=\hat{R}} \tag{11}$$

which further develops to:

$$\dot{\hat{P}}_{gas} = 3 \frac{1}{\Theta_D} \frac{\hat{\rho}_{melt}}{\hat{R}^3} \left(\hat{r}^2 \hat{D} \frac{\partial C}{\partial \hat{r}} \right)_{\hat{r}=\hat{R}} - 3 \hat{P}_{gas} \frac{\dot{\hat{R}}}{\hat{R}} \tag{11a}$$

The number Θ_D may vary by several orders of magnitude, and is typically smaller than one.

The equation of volatile transfer (Eq. 6) transforms to:

$$\Theta_D \frac{dC}{d\hat{t}} = \frac{1}{\hat{r}^2} \frac{\partial}{\partial \hat{r}} \left(\hat{r}^2 \hat{D} \frac{\partial C}{\partial \hat{r}} \right) \tag{12}$$

When diffusion is fast relative to decompression rate, $\Theta_D \ll 1$, the left hand side of Eq. 12, vanishes, and concentration distribution is quasi-static. The equation of diffusion reduces to its steady state form:

$$\frac{1}{\hat{r}^2} \frac{\partial}{\partial \hat{r}} \left(\hat{r} \hat{D} \frac{\partial C}{\partial \hat{r}} \right) = 0 \tag{12a}$$

Quasi-static conditions are expected to be in dome building situations and other relatively slow flowing magma.

The equation of volatile conservation (Eq. 8) transfers to:

$$\hat{R}^3 \hat{P}_{gas} + 3 \hat{\rho}_{melt} \int_{\hat{R}}^{\hat{S}} \hat{r}^2 C d\hat{r} = \frac{S_0^3}{R_i^3} C_0 \hat{\rho}_{melt} \tag{13}$$

The solubility law in its non-dimensional form is:

$$\frac{C_R}{C_i} = \hat{P}_{gas}^n \tag{14}$$

The solubility of water in silicic melt is closely approximated by $n \cong 0.5$, and K_H is typically constant when temperature is constant and pressure rage is limited (Holtz et al., 1996).

3.3. Viscosity controlled growth regime

At the initial stages of growth, when bubbles are small and diffusion is fast enough relative to decompression and to the viscous resistance, gas pressure remains close to its initial value, which is the sum of initial ambient pressure and surface tension:

$$\hat{P}_{gas} \cong 1 + \frac{\Sigma}{\hat{R}} \tag{15}$$

which is practically: $\hat{P}_{gas} \cong 1$. Overpressure in this case increases with falling ambient pressure. Under these conditions, volatile concentration is nearly uniform throughout the melt, thus viscosity is uniform as well. Substituting Eq. 15 (including surface tension) and Eq. 10 into Eq. 9, reduces it to:

$$\Theta_V \frac{\dot{\hat{R}}}{\hat{R}} = \hat{t},\ \hat{R}(\hat{t}=0)=1 \tag{16}$$

Integration of Eq. 16 yields the viscosity controlled growth law:

$$\hat{R} = exp\left(\frac{\hat{t}^2}{2\cdot\Theta_V}\right) \tag{17}$$

This solution is valid as long as the diffusive influx is fast enough to keep gas pressure close to the initial pressure. Pressure relaxation is controlled by $\sqrt{\Theta_V}$. If $\hat{t} \ll \sqrt{\Theta_V}$ (i.e. $t \ll \sqrt{\tau_{vis}\cdot\tau_{dec}}$), then gas pressure is expected to be close to the initial pressure. At this stage growth is exponential so it is initially very slow (equivalent to the time delay of Proussevitch and Sahagian, 1998). At longer times, exponential bubble growth is fast and the diffusive flux into the bubble cannot keep pace with expansion of the bubble and the continuous drop of ambient pressure and Eq. 17 no longer holds.

3.4. Diffusive growth regime

Once diffusion cannot keep up with expansion, gas pressure relaxes and closely follows ambient pressure (Eq. 10):

$$\hat{P}_{gas} \cong 1-\hat{t} \tag{18}$$

Here we assume that bubbles are already large enough to neglect surface tension. The concentration at the bubble–melt interface is thus obtained by substituting Eq. 18 into Eq. 14:

$$C(\hat{r}=\hat{R}) = C_i\sqrt{1-\hat{t}} \tag{19}$$

In these conditions, bubble growth is governed by the diffusive flux of volatiles into the bubble and by the rate of decompression, as it is expressed by substituting Eq. 18 into Eq. 11a:

$$-1 = 3\frac{\hat{\rho}_{melt}}{\Theta_D}\frac{\left(\hat{r}^2\hat{D}\frac{\partial C}{\partial \hat{r}}\right)_{\hat{r}=\hat{R}}}{\hat{R}^3} - 3(1-\hat{t})\frac{\dot{\hat{R}}}{\hat{R}} \tag{20}$$

Here diffusivity varies as a function of volatile concentration, which varies radially. When diffusion is quasi-static, the total mass flux through spherical shell is uniform (Eq. 12a). Integration of Eq. 12a from the outer part of the shell to the bubble–melt interface ($C(\hat{r}=\infty)$ and $C(\hat{r}=\hat{R}) = C_i\sqrt{1-\hat{t}}$) yields:

$$\hat{r}^2\hat{D}\frac{\partial C}{\partial \hat{r}} = \hat{R}\int_{C_i\sqrt{1-\hat{t}}}^{C_i}\hat{D}dC \tag{21}$$

Substituting of Eq. 211 into Eq. 20 yields the law for bubble growth during decompression when viscosity is unimportant and diffusion is quasi-static:

$$\dot{\hat{R}}^2 = \frac{2}{3}\frac{\hat{R}^2}{1-\hat{t}} + 2\frac{\hat{\rho}_{melt}}{\Theta_D}\frac{1}{1-\hat{t}}\int_{C_i\sqrt{1-\hat{t}}}^{C_i}\hat{D}dC \tag{22}$$

For constant diffusivity, integration yields:

$$\hat{R} = \sqrt{\frac{3}{7}\frac{\hat{\rho}_{melt}}{\Theta_D}C_i\left[3(1-\hat{t})^{-\frac{2}{3}} - 7 + 4\sqrt{1-\hat{t}}\right] + (1-\hat{t})^{-\frac{2}{3}}} \tag{23}$$

For variable diffusivity, approximated using a polynomial $\hat{D} = 1+h(C^k - C_i^k)$ where k is the degree of the polynomial and h is constant, the integral at Eq. 22 is:

$$\int_{C_i\sqrt{1-\hat{t}}}^{C_i}\hat{D}dC = C_i\left[1-\sqrt{1-\hat{t}} - hC_i^k\left\{1-\sqrt{1-\hat{t}} - \frac{1}{k+1}\left(1-(1-\hat{t})^{(k+1)/2}\right)\right\}\right] \cong C_i\frac{\hat{t}}{2} \tag{24}$$

To a good approximation, this solution is independent on the choice of h and k, thus Eqs. 20 and 22 are independent of the variations of diffusivity. It means that Eq. 23 is a close approximation for diffusive bubble growth even for variable diffusivity, as long as diffusion is quasi-static. The radial decrease of diffusivity towards the bubble is compensated by an increase of the concentration gradient so that the mass flux is uniform along the profile and is controlled by the value of diffusivity at the outer shell S. However, the decrease of the value of diffusivity near the bubble wall means that quasi-static diffusion will be reached after longer time. The time it takes to reach quasi-static diffusion may be obtained by comparing the concentration gradient for a solitary bubble in a quasi-static case with the non-quasi-static case. The quasi-static diffusion gra-

dient for a solitary bubble is obtained by Eqs. 12a and 14 (Lyakhovsky et al., 1996):

$$\left(\frac{\partial C}{\partial \hat{r}}\right)_{\hat{R}} = C_i \frac{1-\sqrt{\hat{P}_{gas}}}{\hat{R}} \tag{25}$$

The non-quasi-static diffusion gradient, is (Carslaw and Jaeger, 1959):

$$\left(\frac{\partial C}{\partial \hat{r}}\right)_{\hat{R}} = C_i \frac{1-\sqrt{\hat{P}_{gas}}}{\hat{R}} \left(1-\sqrt{\frac{\Theta_D}{\pi}\frac{\hat{R}^2}{\hat{t}}}\right) \tag{26}$$

Thus the conditions for quasi-static diffusion are reached when $\hat{t} > (\Theta_D/\pi)\hat{R}^2$.

3.5. Equilibrium solution

Bubbles reach their largest size at any given ambient pressure when the system is close to mechanical and chemical equilibrium, i.e. when gas pressure follows ambient pressure (Eq. 18) and concentration at the melt shell is uniform according to the solubility at ambient pressure (Eq. 19). Substituting these conditions into Eq. 13) and integrating yields the equilibrium growth law:

$$\hat{R} = \frac{S_0}{R_i}\left(\hat{\rho}_{melt}\frac{C_0 - C_i\sqrt{1-\hat{t}}}{1-\hat{t}}\right)^{\frac{1}{3}} \tag{27}$$

C_0 is the concentration of the melt when the bubble vanishes and S_0 is the cell size when the bubble disappears.

3.6. Transition from high- to low-overpressure growth regimes

The transition from high- to low-overpressure growth regimes depends on the three major processes (diffusion, viscous deformation and decompression). To account for the interplay of the three processes we solve the equations of viscous resistance (Eq. 9) and mass balance (Eqs. 11a and 12a). Substitution of Eqs. 9 and 25 into Eq. 11a) yields the equation for the evolution of gas pressure:

$$\dot{\hat{P}}_{gas} = 3\frac{\hat{\rho}_{melt}C_i}{\Theta_D}\frac{1-\sqrt{\hat{P}_{gas}}}{\hat{R}^2} - \frac{3}{\Theta_V}\hat{P}_{gas}(\hat{P}_{gas}-1+\hat{t}) \tag{28}$$

By using Eq. 25 we assume quasi-static diffusion, where the deviation from quasi-static conditions is given in Eq. 26. The solution is a function of the radius of the bubble. At the initial stages of growth, $\hat{t} < \sqrt{\Theta_V}$, Eq. 17 is a close approximation for bubble radius. Later on, when $\hat{t} > \sqrt{\Theta_V}$, it is an over estimation for bubble radius, however the effect on the calculated pressure is practically negligible, for example when using the diffusive solution Eq. 23 in Eq. 28 yields the same results.

Solutions of Eq. 28 are demonstrated in Fig. 2, which plots the evolution of gas pressure with time as function of the dimensionless parameters Θ_D and Θ_V ($\rho_{melt}C_i$ is of the order of one). When the time of viscous relaxation is short compared with the decompression time (low Θ_V, Fig. 2a), then gas pressure relaxes at the very beginning of decompression, even when diffusion is very effective (e.g. $\Theta_D = 0.0001$). However, for higher Θ_V values the bubbles are overpressed even when diffusion is ineffective (Fig. 2b). Fig. 2c,d shows that gas overpressure depends on both diffusion and viscous resistance, which are represented by the parameters Θ_V and Θ_D. For example, in the case of no mass flux pressure drops at $\Theta_V \sim 1$, whereas in case of fast diffusion ($\Theta_D = 0.0001$) pressure drops in Θ_V values that are 2–3 orders of magnitude lower. Pressure drops from 95 to 5% of the difference $P_{gas} - P_{amb}$ along the Θ_V range of up to 3 orders of magnitudes.

The dependence of gas overpressure on the diffusive, viscous and decompression effects is demonstrated in Fig. 3, which plots the state of the bubbly magma in a Θ_D vs. Θ_V plot. The field of high overpressure ($>95\%$ of the difference $P_{gas} - P_{amb}$, *viscous regime*) is bounded by a curve that is constructed from Fig. 2 (squares and circles for $\hat{t} = 0.05$, 0.5, respectively). The fields of no-overpressure are bounded similarly. For low Θ_V (< 0.0001) gas pressure is relaxed regardless Θ_D, however dehydration of the melt depends on Θ_D and the diffusion scale (S_0 normalized to R_i). The transition from equilibrium to diffusion occurs at $\hat{t} \sim \Theta_D(S_0^2/R_i^2)$. The diffusive growth is quasi-static when $\Theta_D < \pi\hat{t}$.

Equilibrium degassing is obtained when gas pressure is relaxed, as is shown above, and when

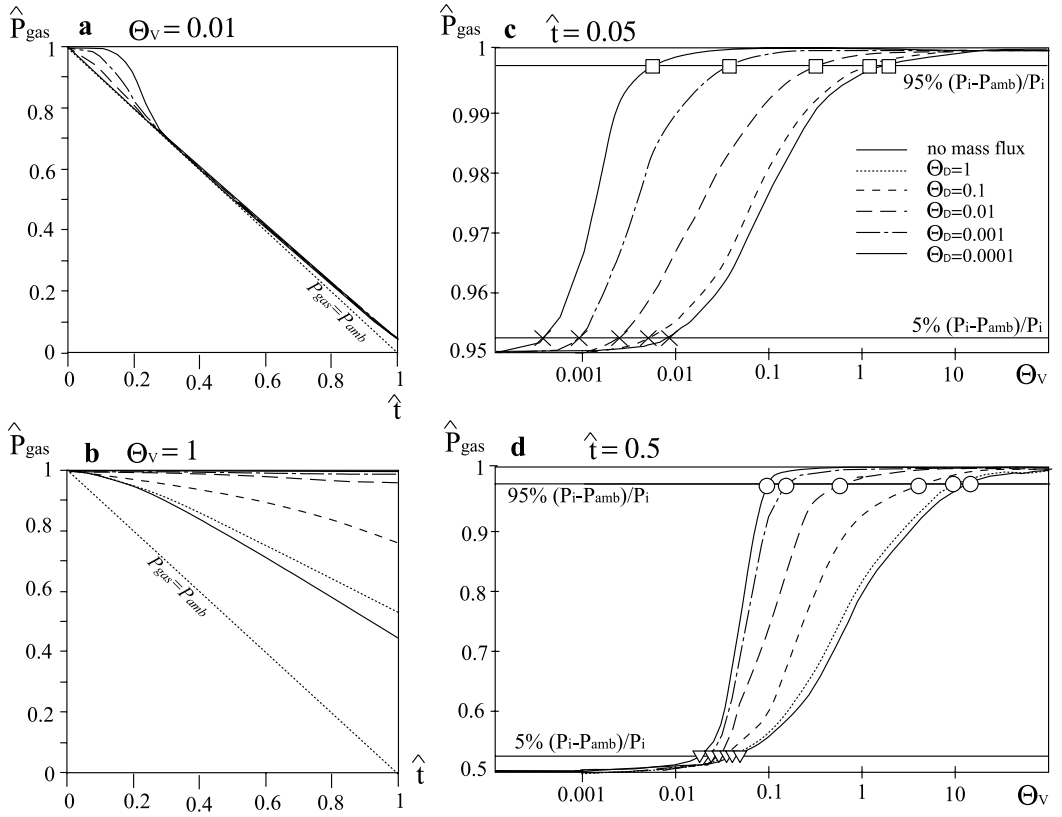

Fig. 2. (a,b) Evolution of gas pressure, legend in (c). Gas pressure is presented vs. time (both dimensionless) for various values of diffusion/decompression ratio, Θ_D, and for viscous/decompression ratio $\Theta_V = 0.01$ (a) and $\Theta_V = 1$ (b). The contribution of diffusive flux to the preservation of gas pressure is clear compared to the case of no mass flux (nmf). The curves are solutions of Eq. 28. (c,d) Gas pressure vs. viscous/decompression ratio, Θ_V. Gas pressure is plotted for various Θ_D values and for $\hat{t} = 0.05$ (c) and 0.5 (d). Depending on the efficiency of diffusion, Θ_D, the viscosity/decompression ratio (Θ_V) in which pressure drops varies few orders of magnitude.

diffusion is fast enough to degas the melt shell. The time to diffuse volatile from the outer cell boundary is estimated by the length of diffusion, which is $S-R<S_0$. Thus, if gas pressure is relaxed, then equilibrium is attained when $\hat{t}>\Theta_D(S_0^2/R_i^2)$.

In some cases the above analytical approximations are not applicable, for example, in the transitions between the solutions and when the shells are thin. To account for the effects that were neglected in the asymptotic solutions, we use a numerical code that solves the full set of equations described in Section 2. The numerical model is based on Lyakhovsky et al. (1996), and allows for variable pressure, diffusivity, and viscosity.

3.7. No volatile mass flux solution

When the diffusive mass flux is insignificant, $\Theta_D \gg 1$, Eqs. 11a and 9) yields the equation of viscous relaxation under decompression:

$$\dot{\hat{P}}_{gas} = -\frac{3}{\Theta_V}\hat{P}_{gas}\left(\hat{P}_{gas} - 1 + \hat{t} - \Sigma\hat{P}_{gas}^{1/3}\right) \qquad (29)$$

Viscosity is uniform and volume fraction is small ($\alpha \ll 1$). Substituting the no mass flux condition, $\hat{P}_{gas}\hat{R}^3 = 1$, into Eq. 29 yields:

$$\dot{\hat{R}} = \frac{1}{\Theta_V}\left(\frac{1}{\hat{R}^2} - \hat{R}(1-\hat{t}) - \Sigma\right) \qquad (30)$$

Bubble size and gas pressure are obtained as function of time for a given decompression rate

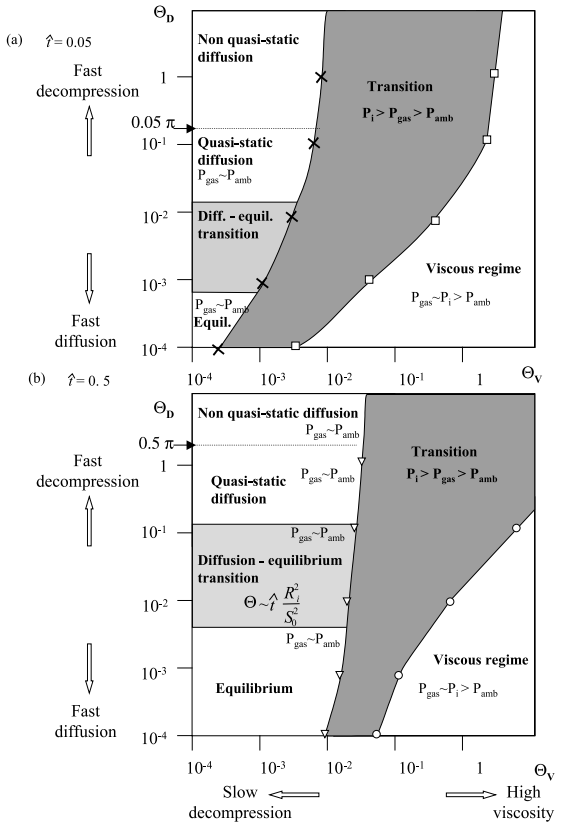

Fig. 3. The bubble growth regime of decompressing magma as function of the two governing parameters, Θ_D and Θ_V at two times, (a) $\hat{t}=0.05$, and (b) $\hat{t}=0.5$. The transition from the overpressed bubbles (viscous regime) to relaxed bubbles (dark gray area) is bounded by two curves that represents 95% and 5% of the pressure difference $P_{gas}-P_{amb}$ (see Fig. 2 with same markers: cross, circle, square and triangle). Gas pressure almost equals the ambient pressure slightly higher in all the fields left from the 'transition' zone. For low Θ_V (<0.0001) gas pressure is relaxed regardless Θ_D, however degassing of the melt depends on Θ_D and the diffusion scale (S_0 normalized to R_i). The transition from equilibrium growth regime to diffusion controlled regime occurs at $\hat{t} \sim \Theta_D(S_0^2/R_i^2)$. The diffusive growth is quasi-static when $\Theta_D < \pi\hat{t}$. The field of equilibrium grows with time at the expanse of both the diffusion regime and viscous regime.

and initial conditions. This solution is similar to equation 18 in Barclay et al. (1995). The no volatile mass flux regime (Eq. 30) is applicable when the decompression time is very short ($\tau_{dec} \ll \tau_{dif}$) and viscosity is high (upper right corner in Fig. 3), which may occur if highly viscous silicic magma is rapidly decompressed.

4. Experimental verification of the model

4.1. Diffusion and equilibrium growth – experiments, analytical and numerical solutions

We designed a new experiment in order to test the analytical and numerical model solutions under the conditions of diffusion and equilibrium regimes.

4.1.1. Experimental procedure

The experimental procedure is presented in Fig. 4. A 1-mm-thick slab of obsidian from Little Glass Butte (LGB), Oregon, was hydrated for 3 days at 850°C and $P_0 = 150$ MPa in a rapid-quench cold-seal pressure vessel (see Hurwitz and Navon, 1994 for description of sample and of procedure). The sample was then decompressed to $P = 111$ MPa in order to nucleate bubbles and cooled to $T = 700$°C. The sample remained in the above conditions for half an hour and the bubbles reached their equilibrium size. At this stage the sample reached the initial conditions for the next stage of the experiment, the decompression stage. The sample was then quenched, taken out and photographed to obtain the initial parameters for the decompression stage, radius and shell size, for as many bubbles as possible. A total of 100 photos were taken to cover the surface of the sample, 2×4 mm from 5 depth layers.

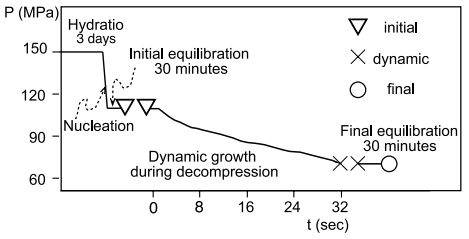

Fig. 4. Experimental procedure. Hydration: 3 days at 850°C and 150 MPa. Nucleation and initial equilibrium: pressure drops to 111 MPa, cooling to 700°C and equilibration for 30 min. Sample was quenched, photographed (triangle, Fig. 5) and reloaded to exactly the same conditions and a few minutes waited to allow thermal and structural relaxation of the sample. Decompression: pressure drops over 32 s to 70 MPa at 700°C, immediate quenching and documenting (cross). Final equilibrium: at 70 MPa, 700°C for 30 min to allow bubble growth to equilibrium, quenching and final documentation (circle).

Having the photographic documentation at hand, we reloaded the sample and brought it back to the previous conditions (111 MPa, 700°C) for half an hour to allow bubbles to return to equilibrium. At the second stage of the experiment we decompressed the sample in a nearly constant decompression rate over 32 s, from $P_i = 111$ MPa to $P_f = 70$ MPa and quenched. Repeating the documentation procedure, we were able to identify bubbles recorded at the previous stage in about 15 frames. By comparing the figures from the two stages, we obtained the amount of growth during non-equilibrium decompression. To verify that the bubbles did not equilibrate during decompression, we reloaded it to the final pressure of the second stage, P_f, and allowed it to reach equilibrium, at this pressure, for 30 min, quenched and photographed. Under the microscope, in spite of reduction of visibility with the increasing gas volume fraction, we succeeded to identify 8 frames identical in location to previous stages.

Using this procedure, we obtained the radii and shell size of individual bubbles in the three stages of experiments (initial equilibrium, dynamic and final equilibrium). This improves the ability to model the data relative to standard techniques, where initial bubble radii are unknown and only the average radius characterizes the dynamic or final stages.

4.1.2. Experimental results

An example of a frame that was photographed in all three stages is shown in Fig. 5. We measured the radii of bubbles that were identified in pictures from the three stages. The measurements are presented in Fig. 6 and in Table 2. Bubbles grew significantly at each of the three stages. This means that starting from initial state in equilibrium, at $P_i = 111$ MPa, bubbles grew in disequilibrium under continuous decompression until quenched at $P_f = 70$ MPa. Then, bubbles continued to grow isobarically until they reached equilibrium at the final pressure. Bubbles radii at the dynamic and final equilibrium stages correlate with the initial radii. This demonstrates that bubble growth is also a function of initial bubble size. Both the initial and final equilibrium radii can be

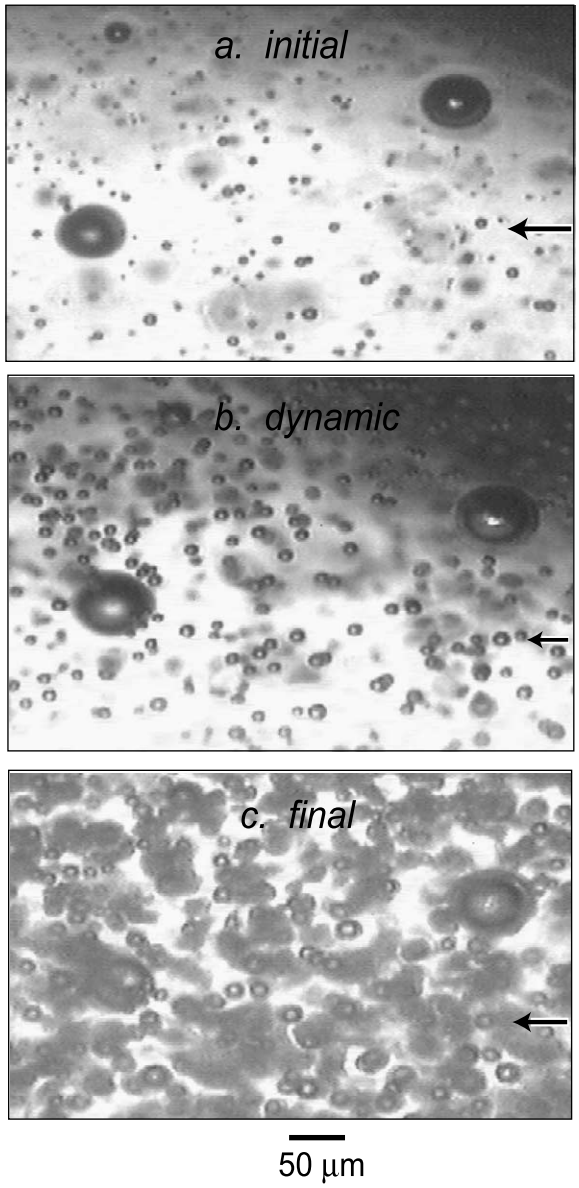

Fig. 5. Microphotographs of water bubbles in rhyolitic glass (experiment NL-526). The three figures show the same region at the three stages. (a) The initial stage is in equilibrium at 700°C and 111 MPa, decompressed from hydration conditions of 850°C and 150 MPa. (b) The dynamic stage of growth was quenched at 700°C and 70 MPa. (c) The final stage is in equilibrium at 700°C and 70 MPa. Arrows indicate a single bubble that is identified in the three experimental stages. For experimental conditions, see text and Fig. 4.

calculated using Eq. 8 for equilibrium conditions ($C = const$ and ρ_{gas} proportional to $P_{gas} = P_{amb}$). The ratio of the equilibrium/initial radii is independent of the initial shell size, S_0:

$$\frac{R_f}{R_i} = \left[\frac{C_0 - C_f}{C_0 - C_i}\frac{P_i}{P_f}\right]^{1/3} \quad (31)$$

The concentrations were calculated using VolatileCalc software (Newman and Lowenstern, 2002): $C_0 = 4.94$ wt%, $C_i = 4.58$ wt%, $C_f = 3.62$ wt%. The calculated ratio, $R_i/R_f = 1.8$, is in agreement with the measured final radii (Fig. 6). This agreement means that the cell model is a reasonable approximation for describing bubble growth. The shell radii calculated based on R_i and R_f are in agreement with radii in the photographs. The few large bubbles (Fig. 5) were not included in the analysis because during the half hour equilibration time additional bubbles nucleated within their shells.

The effect of non-equilibrium growth is evident from the comparison between the radii at the dynamic and final equilibrium stages. The non-equilibrium growth is controlled by the dimensionless numbers Θ_D, Θ_V and $\hat{t}$. The conditions of the decompression experiment are $\Theta_D \sim 1$ and $\Theta_V \sim 10^{-4}$, which, according to Fig. 3, fall in the field of quasi-static diffusion. The diffusion regime solution (Eq. 23) yields a close fit to the measured radii in the dynamic stage (Fig. 6). The numerical simulations yield the same results. Parameters that were used for calculations are $\rho_{melt} = 2300$ kg m^{-3}, decompression rate $\dot{P} = 1.28{\cdot}10^6$ Pa s^{-1}, viscosity according to Hess and Dingwell (1996) (10^6–$2{\cdot}10^6$ Pa s) and diffusivity $D = 1$ μm^2 s^{-1}. The numerical model accounts for variable diffusivity and viscosity (other parameters are mentioned above and initial radii in Table 2). The agreement between the numerical and diffusive analytical solutions assures that

Table 2
Experimental results (NL-526)

Bubble number	Measurements radii (μm)			Calculations radii (μm)		
	R_i[a]	R_d[b]	R_f[c]	R_{num}[d]	R_{dif}[e]	R_{eq}[f]
14w-3	13.0	15.8	20.0	16.1	15.6	22.4
14w-4	7.6	9.6	11.0	10.0	9.5	13.1
14w-7	5.6	8.5	10.6	7.9	7.4	9.6
14w-8	6.5	9.6	12.1	8.8	8.3	11.2
14w-5	6.2	7.8	11.5	8.5	8.0	10.7
14w-6	7.4	9.6	11.8	9.8	9.3	12.7
10x-1	9.3	12.1	14.9	11.9	11.4	16.0
10x-2	7.4	9.6	13.6	9.8	9.3	12.7
10x-3	9.3	11.2	15.0	11.9	11.4	16.0
10x-4	8.7	11.5	14.2	11.3	10.7	15.0
10x-5	5.6	8.7	9.6	7.9	6.5	9.6
10x-6	7.5	10.5	13.0	9.9	9.4	12.9
10x-7	9.0	11.8	15.0	11.6	11.1	15.5
10w-4	8.7	10.2	16.0	11.3	10.7	15.0
10w-5	8.7	11.5	16.0	11.3	10.7	15.0
2b-1	6.8	9.3		9.2	8.7	11.7
2b-2	8.8	10.8		11.4	10.8	15.1
2b-4	10.0	12.7	18.0	12.7	12.2	17.2
2b-5	9.3	11.0	18.0	11.9	11.4	16.0
2b-6	10.2	12.6	18.0	12.9	12.4	17.5

[a] Initial equilibrium radius.
[b] Dynamic radius measured after continuous decompression.
[c] Final equilibrium radius.
[d] Numerical simulation of each bubble, using initial radius (1).
[e] Diffusive bubble growth solution (Eq. 23), using initial radius (1).
[f] Equilibrium growth solution (Eq. 27), using initial radius (1).

growth is indeed governed by the diffusive flux, as is expected from the dimensionless analysis (Fig. 3 and Eq. 28).

4.2. Diffusion controlled growth: experiments and analytical solutions

Gardner et al. (1999) performed controlled decompression experiments in which rhyolitic melts were saturated with water at 200 MPa and 825°C, decompressed to lower pressures at constant rates ranging from 0.025 MPa s^{-1} to 1.0 MPa s^{-1} and then rapidly quenched at various final pressures and documented. They found that at the lower decompression rate (0.025 MPa s^{-1}), melt–vapor equilibrium was maintained over the entire pressure range examined and measured vesicularity reached the expected equilibrium size. At higher decompression rates (0.25–1.0 MPa s^{-1}) equilibrium was not established, bubbles were smaller than expected and volatile content in the melt was higher than the equilibrium values.

According to the dimensionless analysis, the viscous resistance is unimportant even in the higher decompression rate, $\Theta_V < 10^{-5}$ (Fig. 3). Gas pressure is thus expected to relax at the very beginning of decompression long before the first experimental observation ($\hat{t} = 0.1 \gg 10^{-5}$) (Fig. 2). However, the role of diffusion varies according to the decompression rate. In the low decompression rate (0.025 MPa s^{-1}), the dimensionless time for melt depletion is $\Theta_D \cdot S_0^2/R_i^2 < 0.1$, which means that equilibrium is expected to be achieved from the beginning of the decompression, $\bar{t} < 0.1$, as is shown in fig. 7 in Gardner et al. (1999). Diffusion limits the growth of bubbles and the melt remains supersaturated in the faster decompression experiments (0.25–1.0 MPa s^{-1}) since $\Theta_D \cdot S_0^2/R_i^2 > 1$. In Fig. 7 we compare measured radii (from fig. 8 in Gardner et al. (1999)) with the radii calculated according to Eq. 17. The diffusive growth law closely follows the experimental results of decompression rates of 1 MPa s^{-1} (Fig. 7A) and decompression rate 0.25 MPa s^{-1} (Fig. 7B). The initial bubble radius is not known in these experiments, but is expected to be smaller than the first observed radii, which is less than 2 μm. The diffusion solution in these conditions ($R_i < 2$ μm) is not sensitive for the choice of initial bubble radius. The diffusivity that best fits all the data points of the two different decompression rates, 1 $\mu m^2 s^{-1}$ (Fig. 7), is in the order of the diffusivity reported by Zhang and Behrens (2000).

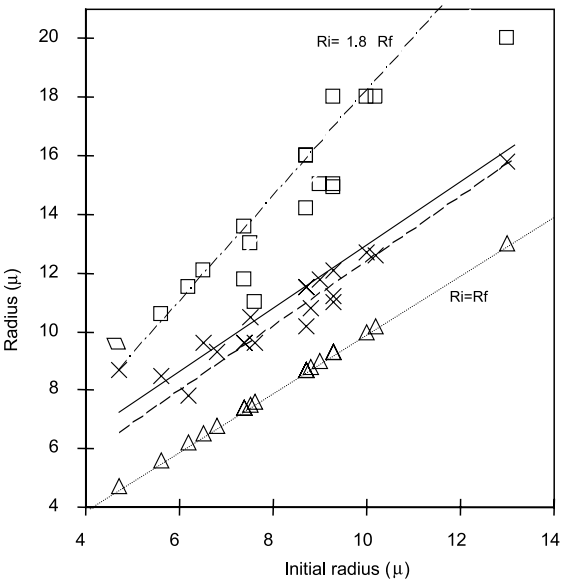

Fig. 6. Bubble radius from the three experimental stages vs. initial bubble radius (Table 2). Bubble size during decompression (crosses) and at final equilibrium (squares) significantly increase with increasing initial bubble size (R_i, triangles), which means that the initial bubble size is an important parameter controlling bubble growth. Three theoretical curves are plotted: the equilibrium growth curve (thin dashed line, Eq. 31), diffusion growth curve (thick line, Eq. 23) and the numerical solution (thick dashed curve), all account for the initial bubble radius.

5. Discussion: gas overpressure in decompressing magmas

The buildup of gas overpressure and supersaturation during magma eruption are major processes controlling the fragmentation of magma. When the viscous resistance of the melt keeps gas pressure above the ambient pressure, the strength of the melt walls between the bubbles may be exceeded and the magma can potentially fragment (Alidibirov and Dingwell, 1996; Mungall et al., 1996; Zhang, 1999). Explosive eruptions are commonly attributed to such a fragmentation mecha-

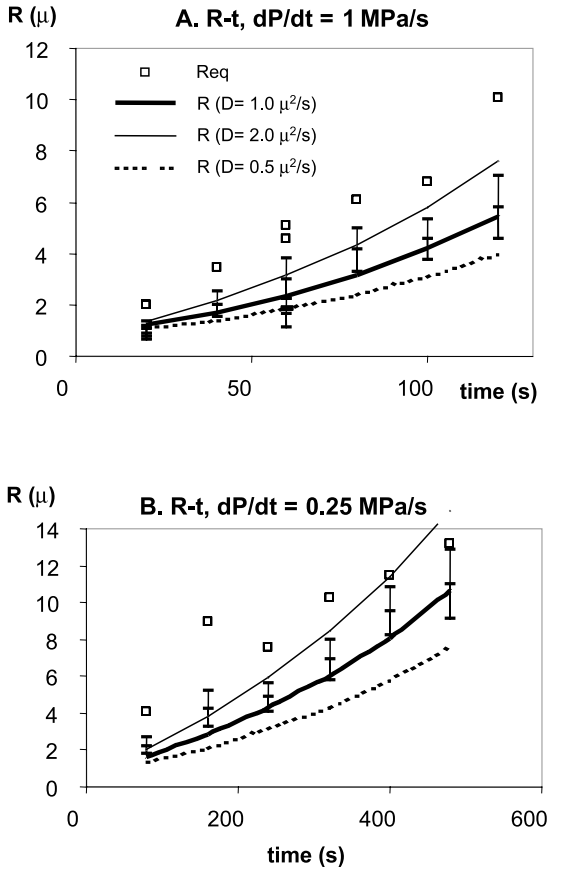

Fig. 7. Variations of bubble radius vs. time in experimental suites of (A) 1.0 MPa s^{-1}, and (B) 0.25 MPa s^{-1} (for the source of data, see Gardner et al. (1999)). Open squares represent the expected equilibrium radius according to Eq. 27 and curves showing the diffusive solution Eq. 23. The thick curve represents the diffusive regime solution where the value of diffusivity (1 μm^2 s^{-1}) was fitted for both sets (A and B). Thin and dashed curves are solutions for diffusivity of 1.0 μm^2 s^{-1} and 0.1 μm^2 s^{-1}, respectively.

nism (Sparks, 1978; Wilson et al., 1980). As shown above, the buildup of gas pressure and supersaturation of erupting magma depend on the interplay of the three dynamic processes (decompression of magma, diffusion of volatiles and viscous deformation of the melt). We compare the predictions of gas overpressure, based on the analytical solutions, with observations from two eruption styles in silicic volcanoes.

Explosive Plinian eruptions are characterized by fast decompression rates. Sparks et al. (1994) estimated that in the violent explosive eruption of Mount St. Helens (18 May 1980), the time scale for the main degassing was tens of seconds or even less. The viscous time scale is estimated to be of the same order of magnitude ($\eta \sim 10^7$–10^8 Pa s, $P_i \sim 10^7$–10^8 Pa), thus the dimensionless ratio of the time scales, Θ_V, is in the order of 0.1–10. The diffusion time scale is also estimated as tens of seconds ($R_i \sim 10$ μm, $D \sim 10^{-11}$ m^2 s^{-1}), thus Θ_D is also of the order of one. Fig. 8 demonstrates that the eruption conditions fall in the transition from high to low overpressure, where bubbles are overpressed and the fragmentation threshold may be exceeded. New bubbles may nucleate in the supersaturated melt surrounding the overpressured bubbles. Due to their smaller size and correspondingly higher Θ_D, their gas pressure is higher and they are more likely to explode.

We now examine the case of steady flow in the deeper part of the conduit during steady Plinian eruption. Here, $\tau_{vis} = 4\eta/P_i$, and $\tau_{dec} = H/V$ where H is the depth of initial saturation and V is the ascent rate. Thus, the dimensionless number related to viscosity is:

$$\Theta_V = \frac{4\eta V}{P_i H} \tag{32}$$

Note that if conduit flow can be approximated by Poiseuille flow (i.e. the volume increase of magma due to bubble growth is small and viscosity is constant), then $V = (4\Delta P/\eta)(a^2/H)$, and Eq. 32 simplifies to $\Theta_V = a^2/H^2$, where a is the conduit radius. For a typical conduit geometry, with conduit diameter of the order of a few tens of meters and depth of a few kilometers, $\Theta_V < 10^{-3}$ and, according to Fig. 8, there is no gas overpressure within the bubbles. Towards the fragmentation level, viscosity and ascent rate increase, Θ_V increase accordingly and magma moves to the right hand side of Fig. 8 where gas pressure increase.

Lava domes are normally associated with slow effusion of lava. However, in some cases dome rocks may explode, e.g. Sato et al., 1992, or the whole dome may be destroyed by sudden onset of explosive activity (Sparks, 1997). The conditions preceding such explosions do not differ much

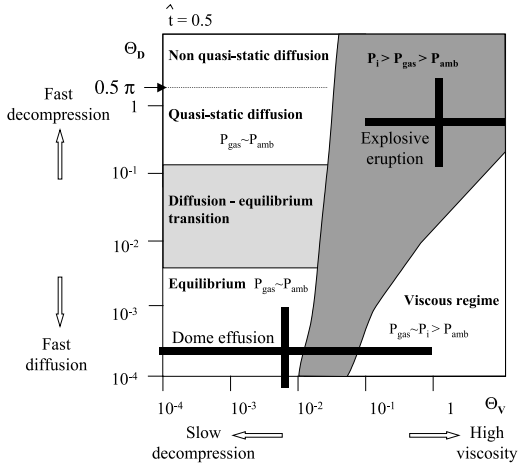

Fig. 8. Conditions of the explosive eruption of Mount St. Helens (18 May 1980) and following effusive dome eruptions plotted on the Θ_D vs. Θ_V diagram. The explosive eruption falls in the transition field where bubbles are overpressed and the melt is supersaturated. The effusive eruptions fall mostly in the equilibrium-degassing field and also in the overpressure growth regime.

from those during magma effusion (Sparks et al., 1994; Sparks, 1997; Melnik and Sparks, 1999). The viscosity of the cooling and partly degassed lava in the dome may be 10^9–10^{13} Pa s and the initial supersaturation pressure is of the order of a few MPa, leading to a viscous time scale of the order of minutes to weeks. The diffusion time is tens to hundreds of seconds. For decompression time of the order of 10^6 s (days to weeks; Sparks et al., 1994), the dimensionless parameters are $\Theta_V \sim 1$–10^{-4} and $\Theta_D \sim 10^{-3}$–10^{-5}. As can be seen in Fig. 8, the dome growth conditions fall mostly in the equilibrium regime. However, when magmas is degassed, Θ_V increases and the magma may migrate towards the explosive regime of Fig. 8 and dome rocks may explode (Sato et al., 1992; Navon et al., 1998). During major dome explosions, a fragmentation wave moves down the conduit, decompression is fast and accordingly Θ_V and Θ_D increase and the magma enters the explosive eruption field at the upper right part of Fig. 8.

During ascent, the ambient pressure monotonically decreases, so that unless decompression is slow enough, the melt is supersaturated. If gas pressure in the bubbles is maintained higher than ambient, it hinders degassing and keeps the melt supersaturated relative to solubility at ambient pressure. Even if gas pressure is relaxed to near ambient, melt away from the bubble may still be supersaturated due to diffusion kinetics. These excess volatiles may pump gas pressure to above ambient if viscosity increases (as in the case of the dome above). Cooling due to exsolution, which becomes significant as magma approaches the vent (Sahagian and Proussevitch, 1996), leads to slowing the diffusive volatile flux and leads to faster release of gas pressure, and on the other hand to viscosity increase and buildup of gas overpressure. Another mechanism that may build gas pressure up is confining the volume of supersaturated magma, e.g. by plugging the conduit. In such a case, gas pressure will increase due to degassing from the supersaturated melt until gas pressure is in equilibrium with the remaining dissolved volatiles in the melt. Pressure buildup in this case is controlled by the rate of volatile diffusion, so the time is roughly the diffusive time scale, τ_{dif}, of the order of minutes. As pressure increases by the continuous addition of volatiles into the melt, it may exceed the strength of the barrier to flow and eruption may continue.

6. Conclusions

(1) The interplay of three dynamic processes controls the growth of bubbles during decompression of hydrated melts: decompression rate, deformation of the viscous melt, and diffusion of the volatile specie from the supersaturated melt into the bubbles. Based on dimensionless analysis, we distinguish three bubble growth regimes. (a) *The viscous regime* appears at the initial stage of decompression when bubbles are small, diffusion is fast and gas pressure remains close to the initial hydration pressure. Overpressure ($P_{gas}-P_{amb}$) continuously increases due to the drop of ambient pressure. (b) *The diffusive regime* occurs when gas pressure follows ambient pressure, but diffusion degassing is not fast enough relative to the buildup of supersaturation with the falling pressure. (c) *Equilibrium* degassing is reached when gas pressure closely approaches am-

bient pressure and diffusion is fast enough to keep melt at supersaturation. We present the analytical solutions of the different growth regimes.

(2) The conditions for each growth regime in decompressing magma are a function of two dimensionless parameters, which are the ratios of diffusive or viscous time scales over the decompression time scale. Using these parameters, Θ_V and Θ_D, it is possible to determine the state of the flowing magma in terms of the three bubble growth regimes.

(3) Experimental results on bubble growth during decompression of hydrated silicic melts were used in order to test the model solutions. The measured radii were successfully fitted by the analytical solutions and by a numerical model.

(4) The model solutions, including the division to the growth regimes as function of the two parameters, provide estimation of the state of erupting magma in terms of gas overpressure, supersaturation and gas volume fraction. The model results are in agreement with the conditions of Plinian explosive eruption (e.g. Mount St. Helens, 18 May 1980), where high gas overpressure is expected. The conditions of effusion of lava domes with sudden onset of explosive activity fall mostly in the regime of equilibrium degassing and partly in overpressure conditions.

(5) We analyze the effect of variable diffusion on bubble growth. In principle, water diffusivity varies with water content. However, we show that in situation of quasi-static diffusion during decompression, the diffusive influx depends on the diffusivity away from the bubble and is not sensitive to the diffusivity profile. The concentration profile adjusts so that the water flux remains uniform and is controlled by the far field flux.

Acknowledgements

Anatoly Chekhmir is greatly acknowledged for assistance in the laboratory experiments. We thank Dork Sahagian for an insightful review that improved the paper. An anonymous reviewer is acknowledged for his careful reading comments and suggesting Eq. 32. We thank Rick Rauenzahn for his comments on Eq. 24. The research was funded by the Israel–US Binational Science Foundation and by the European Community MULTIMO project (EVG1-CT-2000-00021). N.G.L. acknowledges support by the Yeshaya Horowitz Fellowship.

References

Alidibirov, M., Dingwell, D.B., 1996. Magma fragmentation by rapid decompression. Nature 380, 146–148.

Barclay, J., Riley, D.S., Sparks, R.S.J., 1995. Analytical models for bubble growth during decompression of high viscosity magmas. Bull. Volcanol. 57, 422–431.

Blower, J.D., Mader, H.M., Wilson, S.D.R., 2001. Coupling viscous and diffusive controls on bubble growth during explosive volcanic eruption. Earth Planet. Sci. Lett. 193, 47–56.

Burnham, C.W., 1975. Water and magmas; a mixing model. Geochim. Cosmochim. Acta 39, 1077–1084.

Carslaw, H.S., Jaeger, J.D., 1959. Conduction of Heat in Solids. Oxford University Press, Oxford.

Gardner, J.E., Hilton, M., Carrol, M.R., 1999. Experimental constraints on degassing of magma: Isothermal bubble growth during continuous decompression from high pressure. Earth Planet. Sci. Lett. 168, 201–218.

Hess, K.U., Dingwell, D.B., 1996. Viscosities of hydrous leucogranitic melts: A non-Arrhenian model. Am. Mineral. 81, 1297–1300.

Holtz, F., Scaillet, B., Behrens, H., Schulze, F., Pichavant, M., 1996. Water contents of felsic melts: Application to the rheological properties of granitic magmas. Trans. R. Soc. Edinb. (Earth Sci.) 87, 57–64.

Hurwitz, S., Navon, O., 1994. Bubble nucleation in rhyolitic melts: Experiments at high pressure, temperature and water content. Earth Planet. Sci. Lett. 122, 267–280.

Lensky, N., Lyakhovsky, V., Navon, O., 2001. Radial variations of melt viscosity around growing bubbles and gas overpressure in vesiculating magmas. Earth Planet. Sci. Lett. 186, 1–6.

Lyakhovsky, V., Hurwitz, S., Navon, O., 1996. Bubble growth in rhyolitic melts: Experimental and numerical investigation. Bull. Volcanol. 58, 19–32.

Melnik, O., Sparks, R.S.J., 1999. Nonlinear dynamics of lava dome extrusion. Nature 402, 37–41.

Mungall, J.E., Bagdassarov, N.S., Romano, C., Dingwell, D.B., 1996. Numerical modelling of stress generation and microfracturing of vesicle walls in glassy rocks. J. Volcanol. Geotherm. Res. 73, 33–46.

Navon, O., Chekhmir, A., Lyakhovsky, V., 1998. Bubble growth in highly viscous melts: Theory, experiments, and autoexplosivity of dome lavas. Earth Planet. Sci. Lett. 160, 763–776.

Navon, O., Lyakhovsky, V., 1998. Vesiculation processes in silicic magmas. In: Gilbert, J.S., Sparks, R.S.J. (Eds.), The

Physics of Explosive Volcanic Eruptions. Geol. Soc. Spec. Publ. Lond., pp. 27–50.

Newman, S., Lowenstern, J.B., 2002. VolatileCalc: A silicate melt–H_2O–CO_2 solution model written in Visual Basic for Excel. Comput. Geosci. 28, 597–604.

Proussevitch, A.A., Sahagian, D.L., 1996. Dynamics of coupled diffusive and decompressive bubble growth in magmatic systems. J. Geophys. Res. 101, 17447–17455.

Proussevitch, A.A., Sahagian, D.L., 1998. Dynamics and energetics of bubble growth in magmas: Analytical formulation and numerical modeling. J. Geophys. Res. 103, 18223–18251.

Proussevitch, A.A., Sahagian, D.L., Anderson, A.T., 1993. Dynamics of diffusive bubble growth in magmas: Isothermal case. J. Geophys. Res. 98, 22283–22307.

Rayleigh, L., 1917. On the pressure development in a liquid during a collapse of spherical cavity. Philos. Mag. 34, 94–98.

Sahagian, D.L., Proussevitch, A.A., 1996. Thermal effects of magma degassing. J. Volcanol. Geotherm. Res. 74, 19–38.

Sato, H., Fujii, T., Nakada, S., 1992. Crumbling of dacite dome lava and generation of pyroclastic flows at Unzen Volcano. Nature 360, 664–666.

Scriven, L.E., 1959. On the dynamics of phase growth. Chem. Eng. Sci. 10, 1–13.

Sparks, R.S.J., 1978. The dynamics of bubble formation and growth in magmas: A review and analysis. J. Volcanol. Geotherm. Res. 3, 1–37.

Sparks, R.S.J., 1997. Causes and consequences of pressurization in lava dome eruptions. Earth Planet. Sci. Lett. 150, 177–189.

Sparks, R.S.J., Barclay, J., Jaupart, C., Mader, H.M., Phillips, J.C., 1994. Physical aspects of magmatic degassing, 1. Experimental and theoretical constraints on vesiculation. In: Carrol, M.R., Holloway, J.R. (Eds.), Volatiles in Magmas. Rev. Mineral., pp. 413–445.

Toramaru, A., 1989. Vesiculation process and bubble size distribution in ascending magmas with constant velocities. J. Geophys. Res. 94, 17523–17542.

Toramaru, A., 1995. Numerical Study of nucleation and growth of bubbles in viscous magmas. J. Geophys. Res. 100, 1913–1931.

Wilson, L., Sparks, R.S.J., Walker, G.P.L., 1980. Explosive volcanic eruptions – IV. The control of magma properties and conduit geometry on eruption column behavior. Geophys. J. Astr. Soc. 63, 117–148.

Zhang, Y., 1999. A criterion for the fragmentation of bubbly magma based on brittle failure theory. Nature 402, 648–650.

Zhang, Y., Behrens, H., 2000. H_2O diffusion in rhyolitic melts and glasses. Chem. Geol. 169, 243–262.